

EXPERIMENTAL STUDY OF LOAD ALLEVIATION WITH PASSIVE ADAPTIVE CAMBER AIRFOILS

Ayane Sumi[1], Shūji Ōtomo[1] & Hiroyuki Nishida[1]

[1]Department of Mechanical System Engineering, Tokyo University of Agriculture and Technology

Abstract

This study presents a Passive Adaptive Camber (PAC) airfoil equipped with coupled leading- and trailing-edge flaps for load mitigation. The PAC airfoil passively changes its effective camber in response to aerodynamic moments. Its deformation resistance is adjusted using a leaf spring connected to the leading-edge flap. Wind tunnel experiments were conducted under steady-flow conditions to characterize the relationship between passive deformation and lift. A Cauchy number was introduced as a dimensionless measure of the ratio between aerodynamic loading and elastic resistance. The results show that the integrated lift-variation metric depends on the Cauchy number. This trend indicates the existence of an optimal flexibility condition for each angle-of-attack range. The present results provide a design framework for organizing the lift-variation characteristics of a coupled-flap passive camber airfoil using a single dimensionless parameter.

Keywords: Aerodynamics, Load Mitigation, Passive flaps, Passive Adaptive Camber

1. Introduction

Due to the worldwide shift from fossil fuels to renewable energy, research and development have expanded on wind [1, 2] and tidal [3, 4] turbines. To further improve their efficiency, turbine designs must be able to operate effectively across a range of operating conditions, while remaining simple, low-maintenance, and reliable over the long term.

Load mitigation is key to stable and reliable turbine operation. In wind and tidal environments, turbine blades are subjected to highly unsteady inflow caused by gusts [5] and waves [3], the atmospheric [6] and the ocean-bottom [7] boundary layer, yaw misalignment [8, 3], and tower-shadow effects [9, 3]. As a result, the forces on the blades fluctuate periodically or intermittently. These force fluctuations are transmitted through the hub from the blades to the tower and the rest of the support structure, which increases structural damage [10, 11]. Effective mitigation of unsteady loads on turbine blades is therefore essential.

Based on comprehensive reviews [12, 13], Cordes et al. [14] classified turbine load mitigation technologies based on two aspects. The first distinguishes active and passive control based on the use of actuators. The second categorizes approaches as full-blade or sectional-blade concepts. Active strategies offer the advantage of fine adaptation to changing inflow conditions, but they often increase system complexity, power consumption, and maintenance burden. Passive strategies, in contrast, often lack the adaptability and control authority to handle a wide range of flow conditions [15]. However, passive systems avoid control devices and therefore offer structural simplicity. This structural simplicity makes passive concepts attractive for cost-effective turbine designs. For this reason, the present study focuses on a passive approach to blade load mitigation.

A wide variety of active control strategies have been proposed, including several implementations in real turbine systems [16, 17, 18]. Passive concepts have also been proposed in both full-blade and sectional forms. Full-blade passive control is often influenced by the inertia of the entire structure

and is therefore most effective for relatively slow unsteady phenomena. In contrast, sectional approaches involve components with much smaller inertia, allowing even passive systems to achieve high responsiveness and making them suitable for mitigating unsteady load fluctuations over shorter time scales [19].

Representative full-blade passive technologies include passive pitch control. Their effectiveness has been demonstrated through theoretical analyses that provide design guidelines [20]. Numerical simulations have also been conducted to evaluate load mitigation under unsteady inflow conditions [21, 22]. In addition, numerical and experimental studies have been performed on turbine systems close to practical scales [23, 24, 25, 26]. Furthermore, Ness et al. [27] conducted experiments on a turbine equipped with blades that passively twist as a whole, combined with overspeed control, and reported suppression of rotor loads under flow conditions exceeding the rated speed. Similarly, Porter et al. [28] experimentally tested bend–twist composite tidal-turbine blades under combined wave–current loading and showed that the thrust and torque fluctuations per wave cycle were reduced by up to 10% and 14%, respectively, compared with rigid blades.

Typical sectional technologies include airfoils with flexible trailing edges and airfoils equipped with trailing-edge flaps. For example, Cao and Fen [29] experimentally investigated flexible trailing-edge airfoils subjected to sinusoidal vertical gusts and showed that lift fluctuations were mitigated while the mean lift increased compared to rigid airfoils. Maguire et al. [30] proposed a passively morphing blade section with an open flexible trailing edge, in which flexible skins connected to a rigid leading edge are disconnected at the trailing edge. This design allows a large deformation and hence a large load alleviation. Ōtomo et al. [31] subsequently investigated the fluid mechanics of open flexible trailing-edge airfoils and demonstrated that unsteady lift fluctuations can be reduced by up to 52%. For vertical-axis turbines, numerical simulations by Descoteaux and Olivier [32] and experiments by Hoerner et al. [33, 34] have demonstrated the effectiveness of flexible trailing-edge airfoils. On the other hand, Arredondo-Galeana et al. [35] developed a theoretical model for airfoils with passive trailing-edge flaps and showed that load fluctuations induced by angle-of-attack variations can be canceled if the hinge moment is maintained constant. Martínez-Muriel et al. [36] confirmed the mitigation effect of trailing-edge flaps through numerical simulations. These studies indicate that trailing-edge deformation is generally effective for load mitigation in sectional approaches.

Overall, passive trailing-edge deformation has shown promising load-mitigation capability. However, the aerodynamic moment available to drive trailing-edge deformation is generally small. Therefore, this approach requires careful structural design and sufficient flexibility to achieve large deformation amplitudes and effective load mitigation. To overcome this issue, the Adaptive Camber Concept (ACC), featuring mechanically coupled leading- and trailing-edge flaps, was proposed [37, 14]. In the ACC, the large pressure difference across the leading edge rotates the leading-edge flap. This motion is transmitted to the trailing-edge flap through a linkage mechanism, thereby passively modifying the overall airfoil camber. Cordes et al. [14] demonstrated that lift fluctuations induced by wind-direction variations could be reduced by up to 60%.

For passively morphing airfoils to be used as load mitigation devices, their performance must be related quantitatively to design variables. A scaling parameter or design law is therefore needed. For airfoils with deformable trailing edges only, several studies addressing this issue already exist. For example, Arredondo-Galeana et al. [35] suggested that the maximum achievable unsteady load reduction for airfoils with passive trailing-edge flaps is proportional to the ratio of flap length to chord length. In addition, for flexible trailing-edge airfoils, Ōtomo et al. [31] introduced the Cauchy number. This dimensionless parameter represents the ratio of fluid forces to elastic forces, and it was shown to systematically organize the load mitigation and trailing-edge deflection for a wide range of kinematic and flexibility combinations. In contrast, for morphing airfoils such as the ACC that incorporate both leading- and trailing-edge flaps, the framework relating the deformation and load alleviation has not been developed. As a result, the relationship between load mitigation performance and design variables remains unclear. To address this limitation, the present study proposes a newly designed Passive Adaptive Camber (PAC) airfoil. The PAC airfoil follows the fundamental operating principle of the ACC in that it passively deforms in response to changes in the surrounding flow through coupled leading- and trailing-edge flaps. Compared with the ACC, the PAC airfoil increases the design free-

dom by allowing independent adjustment of the flap coupling ratio and the resistance to deformation. The coupling ratio is set by a gear mechanism, whereas the deformation resistance is provided by a leaf spring, as introduced in the next section. To provide a quantitative basis for design, a Cauchy number defined for the PAC mechanism is introduced and used to organize the deformation and aerodynamic responses.

The objective of this study is to experimentally and quantitatively characterize the relationship between passive deformation and aerodynamic response of the newly designed PAC airfoil under static angle-of-attack sweeps. The basic operating principle of the PAC airfoil is based on the Adaptive Camber Concept reported by Cordes et al. [14]. As the first step toward realizing a passive morphing airfoil concept for unsteady load mitigation, this study aims to establish a basis for design guidelines. To this end, we introduce the Cauchy number to characterize the flap deformation and load changes of the PAC airfoil, with spring stiffness treated as a primary design variable. As a preliminary step toward future unsteady experiments, this work focuses on establishing a steady design framework that relates passive deformation and aerodynamic response through a single dimensionless parameter.

This paper is organized as follows: Sect. 2 provides the PAC airfoil concept (Sect. 2.1) and defines the Cauchy number for the PAC airfoil (Sect. 2.2). Sect. 3 provides the experimental details: the airfoil models (Sect. 3.1), wind tunnel setup (Sect. 3.2), and data acquisition procedures (Sect. 3.3). Sect. 4 presents the results and discussion: the measured deformation and lift (Sect. 4.1), and their organization in terms of the Cauchy number (Sect. 4.2). Finally, Sect. 5 summarizes the conclusions and suggests future research directions.

2. Passive adaptive camber (PAC) airfoil concept and Cauchy number

2.1 PAC airfoil concept

Figure 1 illustrates the operating principles of the Passive Adaptive Camber (PAC) airfoil. The geometric definitions for this airfoil are shown in Fig. 2. The PAC airfoil follows the operating principle of the Adaptive Camber Concept proposed by Cordes et al. [14]. The PAC airfoil consists of a leading-edge (LE) flap, a rigid middle section, and a trailing-edge (TE) flap. The LE and TE flaps are mechanically coupled via a gear mechanism, and they rotate in opposite directions. The combined motion of the flaps changes the effective camber of the airfoil.

When the airfoil is in a flow, the aerodynamic moment $M_{\mathrm{aero,LE}}$ acts on the LE flap due to the pressure difference between the suction and pressure sides near the leading edge. This aerodynamic moment rotates the LE flap, and the motion is transmitted to the TE flap through the gear mechanism with a coupling ratio n. Accordingly, the rotation of the LE flap by γ_{LE} induces an opposite rotation of the TE flap given by $\gamma_{\mathrm{TE}} = -n\gamma_{\mathrm{LE}}$. As the TE flap rotates upward, the pressure difference across the airfoil is reduced, which in turn decreases the aerodynamic moment acting on the LE flap. As a result, the LE and TE flaps rotate until the following moment equilibrium is satisfied:

$$M_{\mathrm{aero,LE}} - nM_{\mathrm{aero,TE}} = -\kappa\gamma_{\mathrm{LE}} + M_0, \tag{1}$$

where κ is the torsional spring constant about the LE shaft, and $-\kappa\gamma_{\mathrm{LE}}$ represents the restoring moment acting on the LE flap. Here, M_0 denotes the preload moment required to maintain the initial camber of the airfoil. In this study, the initial camber is set to zero.

The resistance to flap deformation is provided by a leaf spring installed between the LE flap and the middle section (Fig. 1). One end of the leaf spring is inserted into a spring holder fixed to the LE shaft, whereas the other end is supported by the center shaft. As the LE shaft rotates, the leaf spring is loaded at the center-shaft position, and its deformation is approximated as that of a cantilever beam subjected to a concentrated load. Under this configuration, the deformation behavior of the PAC airfoil is governed by the balance between the aerodynamic loading and the elastic restoring force.

2.2 Cauchy number definition for the PAC mechanism

The Cauchy number is a dimensionless parameter that characterizes the deformation of elastic bodies subjected to fluid forces and is widely used in the context of fluid–structure interaction [38, 39, 40, 41, 42, 43, 31]. The present work defines a Cauchy number, Ca, for the PAC airfoil. This parameter

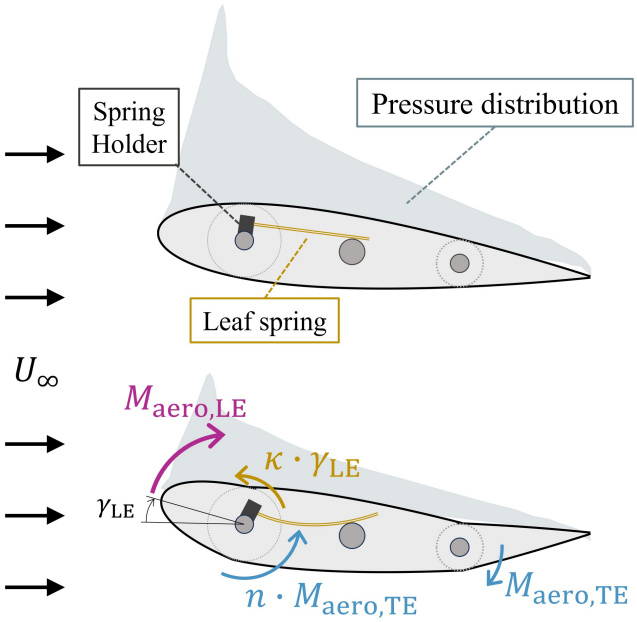


Figure 1 – Operating principle of the Passive Adaptive Camber (PAC) airfoil. The aerodynamic moment acting on the leading-edge flap drives passive rotation, and the motion is transmitted to the trailing-edge flap through a gear mechanism. The coupled flap rotation changes the effective camber of the airfoil. The schematic illustration is inspired by Cordes et al. [14].

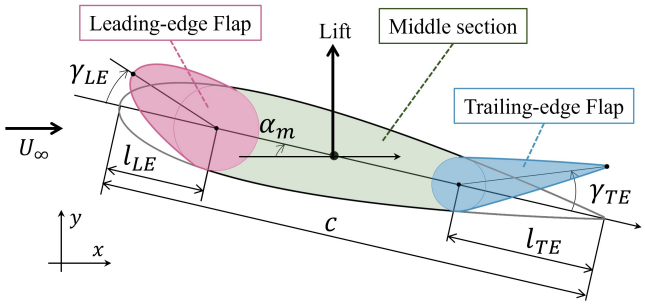


Figure 2 – Geometric definition of the PAC airfoil.

is constructed from the dynamic pressure acting on the flaps and the leaf spring elasticity,

$$Ca = \frac{\rho U_\infty^2 A}{EI/l^2}. \tag{2}$$

The numerator represents a characteristic scale of the aerodynamic force, where ρ is the air density, U_∞ the freestream velocity, and A the projected area of the flaps, defined as $A = (l_{\mathrm{LE}} + l_{\mathrm{TE}})s$, where s is the span. The denominator represents the stiffness of the leaf spring, where E is Young's modulus and I is the second moment of area. For a leaf spring of width b and thickness h, the second moment of area is given by $I = bh^3/12$. Here, l denotes the distance from the fixed end of the spring to the central shaft at which a concentrated load is applied.

3. Experimental Details

3.1 Airfoil model

Two airfoil models were tested: a Passive Adaptive Camber (PAC) airfoil and a rigid airfoil. Both models used a NACA 0018 section, which has been widely employed in turbine-related aerodynamic studies [44, 45, 46, 47]. The chord length was $c = 150$ mm and the span was $s = 392$ mm, corresponding to an aspect ratio of $AR = s/c = 2.61$. The rigid model was fabricated as a monolithic part using stereolithography (SLA) 3D printing.

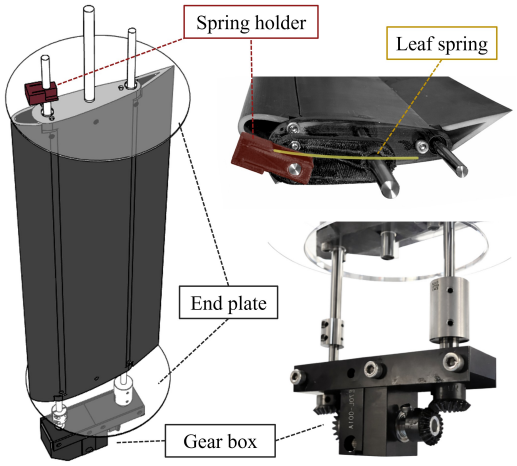


Figure 3 – Passive Adaptive Camber model.

Table 1 – Geometric parameters of the leaf springs and the corresponding Cauchy number.

Length l [mm]	Width b [mm]	Ca [−]
30	4.0	1.6
	8.0	0.7
40	3.0	3.7
	4.0	2.8
	5.0	2.2
	6.0	1.9
	8.0	1.4
50	2.0	8.7
	2.5	7.0
	3.0	5.8
	3.5	5.0
	4.0	4.4
	4.5	3.9
	5.5	3.2
	8.0	2.2

The PAC airfoil model is shown in Fig. 3. The lengths of the LE and TE flaps were $l_{\mathrm{LE}} = 30$ mm $(0.2\ c)$ and $l_{\mathrm{TE}} = 45$ mm $(0.3\ c)$, respectively. The flap length ratios were determined following Cordes et al. [14]. Each of the three components was fabricated as two spanwise halves using SLA 3D printing. The halves were then assembled by adhesive bonding. Clearances of less than 1 mm were provided between the flaps and the middle section to allow smooth rotation. The components were connected via shafts and bearings. The LE and TE shafts had a diameter of 6 mm, whereas the center shaft had a diameter of 8 mm. The LE and TE flaps were mechanically coupled via a gearbox composed of four bevel gears. With the gear ratio fixed at $n = 1$, the flap rotation angle was defined as $\gamma = \gamma_{\mathrm{LE}} = -\gamma_{\mathrm{TE}}$. The maximum allowable deflection was limited by mechanical interference, $\gamma_{\mathrm{Max}} = 40°$.
The deformation resistance was provided by a SUS 304 leaf spring with a thickness of $h = 0.2$ mm and Young's modulus $E = 193$ GPa. The leaf springs were manufactured by electrical discharge machining. In this study, the spring width b and effective length l were varied. Table 1 lists the tested values of b and l and the corresponding Ca calculated by Eq. 2. Figure 4 shows the distribution of Ca over the spring design space (l, b). The tested configurations covered nearly one order of magnitude in Ca. The freestream velocity was fixed at $U_\infty = 7$ m/s for all cases.

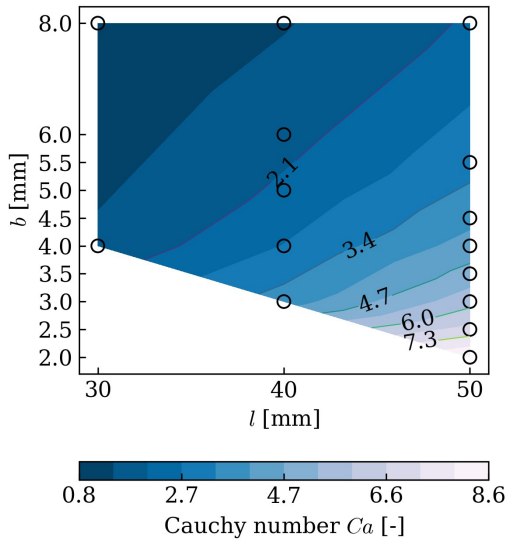


Figure 4 – Contour map of the Cauchy number defined in Eq. 2 over the spring design space (spring length l vs. spring width b). Black circles show tested configurations.

3.2 Experimental setup

Experiments were conducted in the low-speed wind tunnel "SEKILEI" at Tokyo University of Agriculture and Technology. The wind tunnel has a closed test section of $0.4\ \mathrm{m} \times 0.4\ \mathrm{m}$. The contraction ratio is 9:1. At a freestream velocity of $7\ \mathrm{m/s}$, the turbulence intensity is approximately $0.8\ \%$.

The experimental setup is shown in Fig. 5. The airfoil model was mounted at the center of the test section, with the span aligned vertically. The Reynolds number based on the chord length $c = 150\ \mathrm{mm}$ was $Re = 7.0 \times 10^4$. The Reynolds number was selected by considering the stable operating range of the wind tunnel, the measurable force range, and the magnitude of passive deformation. Acrylic end plates with a thickness of $1.5\ \mathrm{mm}$ were attached to both ends of the airfoil. The gaps between the end plates and the upper and lower tunnel walls were $2.5\ \mathrm{mm}$ on each side. The angle of attack of the middle section α_m was controlled by a stepper motor mounted above the model. The value of α_m was swept from 0° to 20° in increments of 1°.

3.3 Data acquisition

Lift and flap deformation data were acquired at a sampling frequency of $1000\ \mathrm{Hz}$ using a National Instruments DAQ system (NI USB-6212), controlled via MATLAB. At each α_m, the system was allowed to settle for $10\ \mathrm{s}$ after changing α_m, followed by a $20\ \mathrm{s}$ measurement period. Time-averaged values were used to represent steady-state conditions. The flap rotation angle γ was measured using a

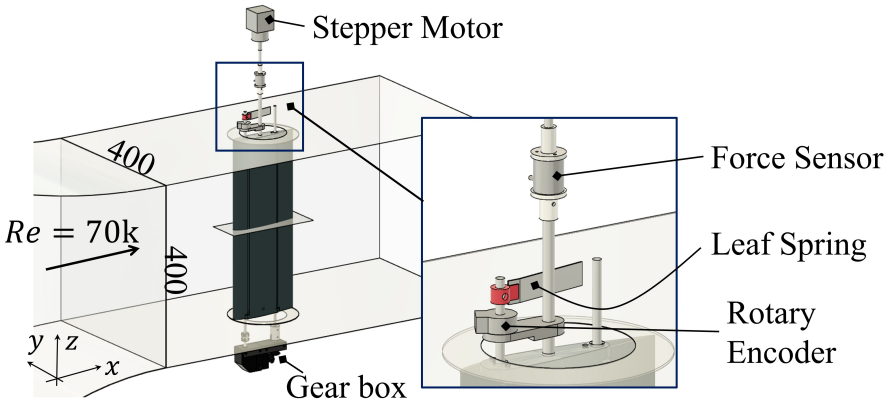


Figure 5 – Experimental setup.

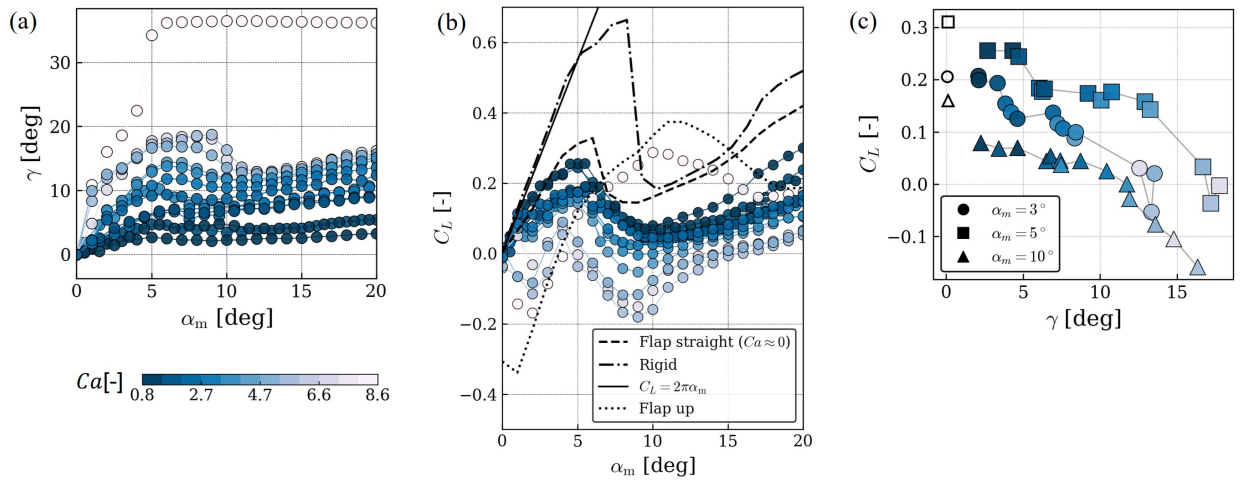


Figure 6 – Measured flap deformation and lift characteristics of the PAC airfoil. (a) Flap rotation angle γ as a function of the angle of attack of the middle section α_{m}. (b) Lift coefficient C_L as a function of α_{m}. (c) Relationship between C_L and γ at selected angles of attack.

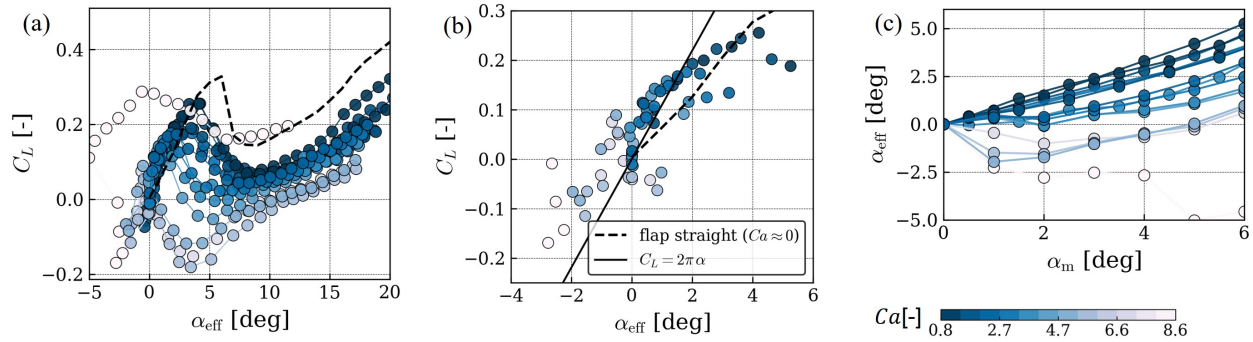


Figure 7 – Lift characteristics organized using the effective angle of attack α_{eff}. (a) Lift coefficient C_L plotted against α_{eff}. (b) Close-up of the low-angle region, where the lift response approximately collapses onto a linear trend. (c) Effective angle of attack α_{eff} plotted against the middle-section angle of attack α_{m} for $0^\circ \leq \alpha_{\mathrm{m}} \leq 6^\circ$.

rotary encoder (Broadcom, AS22-M520-5G12) with a resolution of 360 counts per revolution (CPR), corresponding to an angular resolution of 0.25°. Forces were recorded by a six-axis force sensor (Leptrino, PFS020YA500G6) with a range of ± 50 N and a DAQ-limited resolution of 1.5×10^{-3} N, corresponding to a lift-coefficient resolution of 8.5×10^{-4}. The lift coefficient is defined as

$$C_L = \frac{L}{\frac{1}{2}\rho U_\infty^2 S}, \tag{3}$$

where ρ is the air density and S is the reference area defined as the projected area of the airfoil, $S = cs$. At $\alpha_{\mathrm{m}} = 20\ ^\circ$, the blockage reached approximately 13 %. The freestream velocity U_∞ used in the evaluation of C_L was measured simultaneously using an upstream Pitot tube and a differential pressure transducer.

4. Results and Discussion

4.1 Flap Displacement and Aerodynamic Forces

The measured aerodynamic characteristics of the PAC airfoil are shown in Fig. 6. Figure 6 (a) shows the flap rotation γ against the angle of attack of the middle section α_{m}. Under the largest Ca, γ reaches the maximum deflection $\gamma_{\mathrm{Max}} = 40^\circ$ at $\alpha_{\mathrm{m}} \approx 5\ ^\circ$. For the other Ca conditions, γ varies nonlinearly over α_{m}. The peak γ for each Ca shifts towards higher α_{m} with increasing Ca. In general, γ increases with increasing Ca. This trend indicates that Ca is an effective indicator of the flexibility of the PAC airfoil.

Figure 6 (b) presents C_L against α_{m}. The dash-dotted line shows C_L for the rigid airfoil. The dotted line corresponds to the "flaps up" condition, in which the flaps are fixed at $\gamma_{\mathrm{Max}} = 40^\circ$. The dashed line represents the "flaps straight" condition, in which the flaps are fixed at $\gamma = 0$, corresponding to $Ca \approx 0$. Under the "flaps straight" condition, the stall angle is approximately 6°, and the maximum C_L is about 0.35, both of which are significantly smaller than those of the rigid airfoil. Further analysis, including flow visualization, is needed to clarify the reason for the discrepancy. Possible contributing factors include the surface steps introduced by the flap structure and residual three-dimensional effects. Accordingly, the "flaps straight" condition is used as the baseline in the following analysis. This comparison allows the effect of passive deformation on the lift response to be evaluated separately from the aerodynamic effects of the flap structure itself.

For the smallest Ca, the lift behavior is close to that of the "flaps straight" condition. As Ca increases, the entire C_L–α_{m} curve shifts in the negative direction. At the largest Ca, the lift characteristics approach those of the "flaps up" condition. As shown in Fig. 6 (a), the increase in γ with α_{m} is not monotonic. This behavior of γ corresponds closely to the variation in lift shown in Fig. 6 (b). For example, in PAC airfoils with small Ca, stall occurs around $\alpha_{\mathrm{m}} \approx 5^\circ$. Up to this stall angle, γ increases with increasing α_{m}, resulting in suppression of the peak lift coefficient due to the effect of negative camber. After stall, the aerodynamic moment acting on the leading-edge flap $M_{\mathrm{aero,LE}}$ decreases causing a temporary reduction in γ.

Figure 6 (c) shows the relationship between C_L and γ at $\alpha_{\mathrm{m}} = 3^\circ$, 5°, and 10°, excluding the largest Ca condition. As γ increases, i.e., as the camber becomes more negative, C_L decreases. The C_L–γ curve shows distinct changes in slope. For $\alpha_{\mathrm{m}} = 3^\circ$ and 5°, the slope sharply changes around $\gamma = 5^\circ$ corresponding to the angle of attack of the leading-edge flap $\alpha_{\mathrm{LE}} = 8^\circ$ and 10°. In contrast, no such trend is observed for $\alpha_{\mathrm{m}} = 10^\circ$. The cases at $\alpha_{\mathrm{m}} = 3^\circ$ and 5° corresponds to pre-stall conditions, whereas the case at $\alpha_{\mathrm{m}} = 10^\circ$ corresponds to a post-stall condition. The slope change around $\gamma = 5^\circ$ is therefore likely associated with flow separation near the upper surface of the LE flap. Another slope change is observed around $\gamma = 10^\circ$. This second change may be related to flow separation near the lower surface of the TE flap.

To further interpret these results, the effective angle of attack $\alpha_{\mathrm{eff}} = \alpha_{\mathrm{geo}} - \alpha_{L=0}$ is introduced. Here, α_{geo} denotes the geometric angle of attack, defined as the angle between the chord line and the incoming flow, and $\alpha_{L=0}$ represents the zero-lift angle associated with the airfoil camber. According to thin airfoil theory [48], $\alpha_{L=0}$ is given by

$$\alpha_{L=0} = -\frac{1}{\pi}\int_0^\pi \eta x'(\cos\phi - 1)\phi, \tag{4}$$

where $\eta(x')$ is the camber-line function, ϕ is the Glauert angle, and the chordwise coordinate is related by $x' = c(1-\cos\phi)/2$. In the present analysis, $\eta(x')$ is constructed as a piecewise linear approximation of the airfoil mean camber line.

Figure 7 (a) shows C_L against α_{eff}, Fig. 7 (b) presents a close-up of the low-angle region ($0^\circ \leq \alpha_{\mathrm{m}} \leq 6^\circ$), and Fig. 7 (c) shows α_{eff} against α_{m}. As shown in Fig. 7 (b), particularly in the range of small angles of attack and small deflections, C_L collapses linearly when plotted against α_{eff}. This result indicates that, in the low-angle pre-stall regime, the lift response of the PAC airfoil can be characterized by α_{eff}. Furthermore, Fig. 7 (c) shows that there exists a range of Ca for which α_{eff} is maintained near 0° despite increases in α_{m}. Under such conditions, variations in C_L with respect to α_{m} are suppressed, leading to effective mitigation of lift fluctuations.

4.2 Relationship Between Load Mitigation Effect and the Cauchy Number

To quantify the load mitigation effect in the lift response, the following metric is introduced:

$$J = \int |C_L(\alpha_{\mathrm{m}})|\,\alpha_{\mathrm{m}}. \tag{5}$$

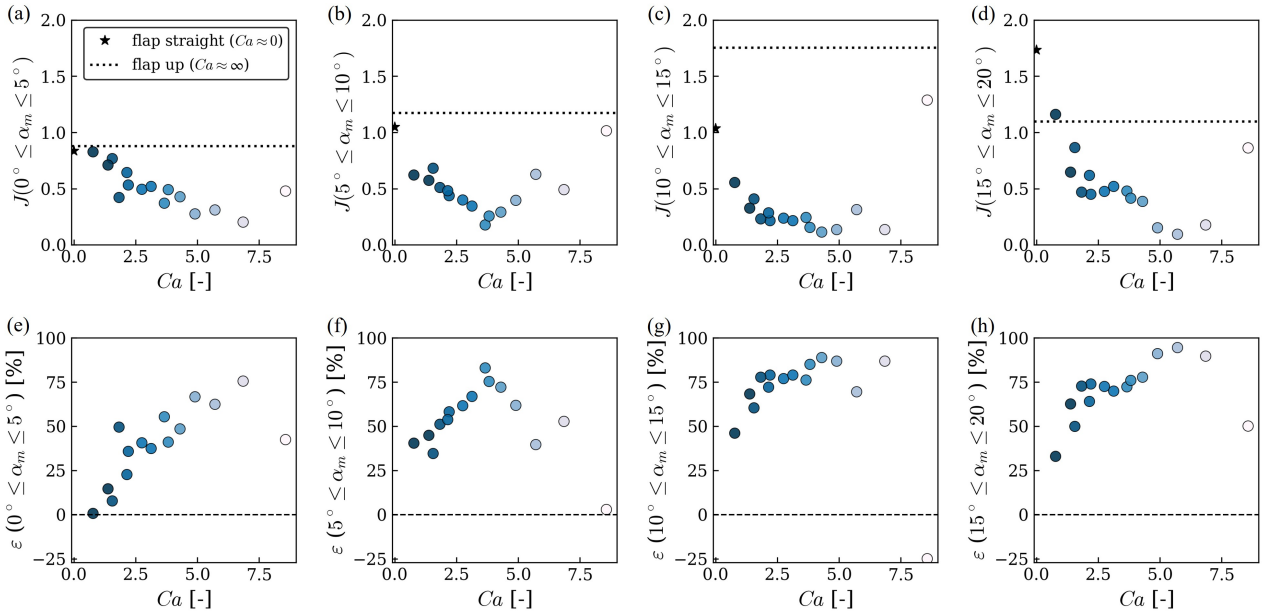


Figure 8 – Integrated lift-variation metric J and reduction rate ε plotted against the Cauchy number Ca. Panels (a)–(d) show J for the angle-of-attack ranges $0^\circ \leq \alpha_\mathrm{m} \leq 5^\circ$, $5^\circ \leq \alpha_\mathrm{m} \leq 10^\circ$, $10^\circ \leq \alpha_\mathrm{m} \leq 15^\circ$, and $15^\circ \leq \alpha_\mathrm{m} \leq 20^\circ$, respectively. Panels (e)–(h) show the corresponding reduction rate ε for the same angle-of-attack ranges.

This metric represents the cumulative deviation of the lift coefficient from the initial reference state $C_L = 0$. In addition, the lift reduction rate ε relative to the "flaps straight" condition is defined as

$$\varepsilon = 1 - \frac{\int |C_L(\alpha_\mathrm{m})|\, \alpha_\mathrm{m}}{\int |C_{L,\mathrm{straight}}(\alpha_\mathrm{m})|\, \alpha_\mathrm{m}}. \tag{6}$$

Figure 8 shows J and ε as functions of the Cauchy number Ca. The integration ranges are as follows: $0^\circ \leq \alpha_\mathrm{m} \leq 5^\circ$ (Figs. (a) and (e)), $5^\circ \leq \alpha_\mathrm{m} \leq 10^\circ$ (Figs. (b) and (f)), $10^\circ \leq \alpha_\mathrm{m} \leq 15^\circ$ (Figs. (c) and (g)), and $15^\circ \leq \alpha_\mathrm{m} \leq 20^\circ$ (Figs. (d) and (h)). For each integration range, an optimal value of Ca exists. At this value, J reaches a minimum and the reduction rate ε reaches a maximum. This indicates that when Ca is too small, the airfoil deformation is insufficient, whereas when Ca is too large, the deformation becomes excessive; in both cases, the load mitigation effect deteriorates.

The optimal Ca also depends on the angle-of-attack range. In the low-angle region ($0^\circ \leq \alpha_\mathrm{m} \leq 5^\circ$) shown in Figs. 8 (a) and (e), the reduction rate is maximized when α_eff remains close to 0°, as expected from Fig. 7 (c). In contrast, in the moderate-angle region ($5^\circ \leq \alpha_\mathrm{m} \leq 10^\circ$) and beyond, the optimal Ca shifts toward stiffer conditions compared to the low-angle region, as shown in Figs. 8 (b) and (f). The present results suggest that excessive deformation does not necessarily provide additional lift reduction. One possible explanation is that, when both the angle of attack and flap deformation are large, the aerodynamic force acting on the leading-edge flap includes a larger drag-direction component. This component tends to further deflect the flap, resulting in excessive deformation. In this regime, sufficient stiffness is therefore required to resist this force. Consequently, the optimal Ca corresponds to more moderate passive deformation.

5. Conclusions

In this study, wind tunnel experiments were conducted under steady-flow conditions using a Passive Adaptive Camber (PAC) airfoil, in which the leading-edge and trailing-edge flaps are mechanically coupled. The deformation resistance was adjusted by a leaf spring connected to the leading-edge flap. The relationship between the airfoil's passive deformation and lift was systematically investigated. In addition, the Cauchy number Ca, the dimensionless parameter representing the ratio of aerodynamic to elastic forces, was introduced as an index of airfoil flexibility.

The experimental results confirmed that the flap rotation angle γ increases with increasing Ca. Accordingly, the lift characteristics transition from the "flaps straight" state to the "flaps up" state. Furthermore, because the lift coefficient C_L decreases as γ increases, γ can be interpreted as an indicator of the effective camber of the airfoil. These findings demonstrate that the aerodynamic response of the PAC airfoil can be organized using the Cauchy number.

By evaluating an integrated lift-variation metric over a range of angles of attack, it was found that the load mitigation effect exhibits an extremum with respect to Ca. This indicates the existence of an optimal flexibility condition. Although the present study is limited to steady-flow conditions, approximately an 80% reduction in lift variation was achieved at the optimal Ca condition relative to the "flaps straight" condition. Since the optimal Ca depends on the angle-of-attack range considered, designing the Cauchy number according to the operating conditions is essential for maximizing the load mitigation performance of the PAC airfoil.

Overall, the relationship between passive deformation and lift in the PAC airfoil was organized using the Cauchy number. This result indicates that effective lift mitigation can be achieved by providing an appropriate level of flexibility. Moreover, the results demonstrate the potential of the Cauchy number as a scaling parameter for the load-mitigation performance of the PAC airfoil.

The present study represents a first step toward realizing a passive morphing airfoil concept for mitigating unsteady loads. Nevertheless, the present investigation is limited to static angle-of-attack sweeps under a single gear ratio. In addition, the influence of the unsteady flows and gust response has not been assessed. Future work will investigate the effects of unsteady flows, gust responses, and gear ratios to further assess the validity of the scaling based on the Cauchy numbers. The framework will be extended to unsteady inflow conditions, such as sinusoidal gusts, to evaluate the unsteady load-mitigation performance.

6. Funding

This work was supported by JSPS KAKENHI Grant No. JP24K17204.

7. Contact Author Email Address

mailto: sumi@st.go.tuat.ac.jp

8. Copyright Statement

The authors confirm that they, and/or their company or organization, hold copyright on all of the original material included in this paper. The authors also confirm that they have obtained permission, from the copyright holder of any third party material included in this paper, to publish it as part of their paper. The authors confirm that they give permission, or have obtained permission from the copyright holder of this paper, for the publication and distribution of this paper as part of the ICAS proceedings or as individual off-prints from the proceedings.

References

[1] Jens Nørkærrkær Sørensen. Aerodynamic aspects of wind energy conversion. *Annual Review of Fluid Mechanics*, 43:427–448, 2011.

[2] Richard J.A.M. Stevens and Charles Meneveau. Flow structure and turbulence in wind farms. *Annual Review of Fluid Mechanics*, 49:311–339, 2017.

[3] Thomas A A Adcock, Scott Draper, Richard H J Willden, and Christopher R Vogel. The fluid mechanics of tidal stream energy conversion. *Annual Review of Fluid Mechanics*, 58:287–310, 2021.

[4] Gang Li and Weidong Zhu. Tidal current energy harvesting technologies: A review of current status and life cycle assessment. *Renewable and Sustainable Energy Reviews*, 179:113269, 2023.

[5] Anya R Jones, Oksan Cetiner, and Marilyn J Smith. Physics and modeling of large flow disturbances: Discrete gust encounters for modern air vehicles. *Annual Review of Fluid Mechanics*, 54:469–493, 2022.

[6] John Roy Garratt. The atmospheric boundary layer. *Earth-Science Reviews*, 37(1-2):89–134, 1994.

[7] John H Trowbridge and Steven J Lentz. The bottom boundary layer. *Annual Review of Marine Science*, 10(1):397–420, 2018.

[8] Rick Damiani, Scott Dana, Jennifer Annoni, Paul Fleming, Jason Roadman, Jeroen Van Dam, and Katherine Dykes. Assessment of wind turbine component loads under yaw-offset conditions. *Wind Energy Science*, 3:173–189, 2018.

[9] Juliet G. Simpson, Meghan Kaminski, and Eric Loth. Influence of tower shadow on downwind flexible rotors: Field tests and simulations. *Wind Energy*, 25:881–896, 2022.

[10] Edward Hart, Benjamin Clarke, Gary Nicholas, Abbas Kazemi Amiri, James Stirling, James Carroll, Rob Dwyer-Joyce, Alasdair McDonald, and Hui Long. A review of wind turbine main bearings: Design, operation, modelling, damage mechanisms and fault detection. *Wind Energy Science*, 5:105–124, 2020.

[11] G. Sieros, P. Chaviaropoulos, J. D. Sørensen, B. H. Bulder, and P. Jamieson. Upscaling wind turbines: theoretical and practical aspects and their impact on the cost of energy. *Wind Energy*, 15:3–17, 2012.

[12] T. K. Barlas and G. A.M. van Kuik. Review of state of the art in smart rotor control research for wind turbines. *Progress in Aerospace Sciences*, 46:1–27, 2010.

[13] CP Van Dam, Dale E Berg, and Scott J Johnson. Active load control techniques for wind turbines. Technical report, Sandia National Laboratories, Albuquerque, NM, USA, 2008.

[14] U. Cordes, B. Lambie, K. Hufnagel, H. Spiegelberg, G. Kampers, and C. Tropea. The adaptive camber concept - a passive approach for gust load alleviation on wind turbines. *Wind Energy*, 21:732–744, 2018.

[15] Mohamad Gad-el Hak. *Flow Control : Passive, Active, and Reactive Flow Management*. Cambridge University Press, 2000.

[16] Xavier Lachenal, Stephen Daynes, and Paul M Weaver. Review of morphing concepts and materials for wind turbine blade applications. *Wind energy*, 16(2):283–307, 2013.

[17] Sandrine Aubrun, Annie Leroy, and Philippe Devinant. A review of wind turbine-oriented active flow control strategies. *Experiments in Fluids*, 58(10):134, 2017.

[18] Md Zishan Akhter and Farag Khalifa Omar. Review of flow-control devices for wind-turbine performance enhancement. *Energies*, 14(5):1268, 2021.

[19] Ignazio Maria Viola, Gabriele Pisetta, Weidong Dai, Abel Arredondo-Galeana, Anna M Young, and Amanda S M Smyth. Morphing blades: Theory and proof of principles. *International Marine Energy Journal*, 5:183–193, 2022.

[20] Shūji Ōtomo, Stefano Gambuzza, Yabin Liu, Anna M. Young, Riccardo Broglia, Edward D. McCarthy, and Ignazio Maria Viola. A general framework for the design of efficient passive pitch systems. *Physics of Fluids*, 36(6), 2024.

[21] Gabriele Pisetta, Robin Le Mestre, and Ignazio Maria Viola. Morphing blades for tidal turbines: A theoretical study. *Renewable Energy*, 183:802–819, 2022.

[22] Yabin Liu, Riccardo Broglia, Anna M Young, Edward D Mccarthy, and Ignazio Maria Viola. Unsteady load mitigation through passive pitch. *Journal of Fluids and Structures*, 131:104216, 2024.

[23] Weidong Dai, Riccardo Broglia, and Ignazio Maria Viola. Mitigation of rotor thrust fluctuations through passive pitch. *Journal of Fluids and Structures*, 112:103599, 2022.

[24] Stefano Gambuzza, Gabriele Pisetta, Thomas Davey, Jeffrey Steynor, and Ignazio Maria Viola. Model-scale experiments of passive pitch control for tidal turbines. *Renewable Energy*, 205:10–29, 2023.

[25] Stefano Gambuzza, Puja Sunil, Mario Felli, Anna M. Young, Riccardo Broglia, Edward D. McCarthy, and Ignazio Maria Viola. Power and thrust control by passive pitch for tidal turbines. *Renewable Energy*, 239:121921, 2025.

[26] Puja Sunil, Kuba Frankowski, Anna M. Young, Michael O'Sullivan, Edward D. McCarthy, Riccardo Broglia, and Ignazio Maria Viola. Role of preload in determining the performance enhancement of tidal turbines by passive pitch. *Renewable Energy*, 256:124698, 2026.

[27] Katherine Van Ness, Alberto Aliseda, and Brian Polagye. Experimental comparison of passive adaptive blade pitch control strategies for an axial-flow current turbine. *Journal of Ocean Engineering and Marine Energy*, 10:105–123, 2024.

[28] Kate E. Porter, Stephanie E. Ordonez-Sanchez, Robynne E. Murray, Matthew Allmark, Cameron M. Johnstone, Tim O'Doherty, Allan Mason-Jones, Darrel A. Doman, and Michael J. Pegg. Flume testing of passively adaptive composite tidal turbine blades under combined wave and current loading. *Journal of Fluids and Structures*, 93:102825, 2020.

[29] Yu Tian Cao and Li Hao Feng. Gust response of an airfoil with a flexible trailing edge. *Physics of Fluids*, 37(1), 2025.

[30] James M. Maguire, Dimitrios Mamalis, Shūji Ōtomo, and Edward D. McCarthy. Passively morphing trailing edge design for composite tidal turbine blades. *Composite Structures*, 337:118090, 2024.

[31] Shūji Ōtomo, Anna M. Young, Edward D. McCarthy, and Ignazio Maria Viola. Scaling unsteady load alleviation in airfoils with flexible trailing-edges. *Physical Review Fluids*, 10(11):114102, 2025.

[32] Pierre Olivier Descoteaux and Mathieu Olivier. Performances of vertical-axis hydrokinetic turbines with chordwise-flexible blades. *Journal of Fluids and Structures*, 102:103235, 2021.

[33] Stefan Hoerner, Cyrille Bonamy, Olivier Cleynen, Thierry Maître, and Dominique Thévenin. Darrieus vertical-axis water turbines: deformation and force measurements on bioinspired highly flexible blade profiles. *Experiments in Fluids*, 61(6):141, 2020.

[34] Stefan Hoerner, Shokoofeh Abbaszadeh, Olivier Cleynen, Cyrille Bonamy, Thierry Maître, and Dominique Thévenin. Passive flow control mechanisms with bioinspired flexible blades in cross-flow tidal turbines. *Experiments in Fluids*, 62(5):104, 2021.

[35] Abel Arredondo-Galeana, Anna M. Young, Amanda S.M. Smyth, and Ignazio Maria Viola. Unsteady load mitigation through a passive trailing-edge flap. *Journal of Fluids and Structures*, 106:103352, 2021.

[36] C. Martínez-Muriel, I. M. Viola, M. García-Villalba, and O. Flores. Mitigating unsteady loads at low reynolds numbers using a passive trailing-edge flap. *Journal of Fluids and Structures*, 138:104392, 2025.

[37] Benjamin Lambie. *Aeroelastic Investigation of a Wind Turbine Airfoil with Self-Adaptive Camber*. PhD thesis, Technische Universität Darmstadt, Germany, 2011.

[38] Emmanuel de Langre. Effects of wind on plants. *Annual Review of Fluid Mechanics*, 40:141–168, 2008.

[39] D. Ishihara, Y. Yamashita, T. Horie, S. Yoshida, and T. Niho. Passive maintenance of high angle of attack and its lift generation during flapping translation in crane fly wing. *Journal of Experimental Biology*, 212:3882–3891, 2009.

[40] Frdrick Gosselin, Emmanuel De Langre, and Bruno A. MacHado-Almeida. Drag reduction of flexible plates by reconfiguration. *Journal of Fluid Mechanics*, 650:319–341, 2010.

[41] Yaqing Jin, Jin Tae Kim, Shifeng Fu, and Leonardo P. Chamorro. Flow-induced motions of flexible plates: Fluttering, twisting and orbital modes. *Journal of Fluid Mechanics*, 864:273–285, 2019.

[42] Tom Marzin, Emmanuel De Langre, and Sophie Ramananarivo. Shape reconfiguration through origami folding sets an upper limit on drag. *Proceedings of the Royal Society A*, 478(2267), 2022.

[43] Tristan Aurégan, Benjamin Thiria, Sylvain Courrech, Du Pont, and Sylvain Courrech Du Pont. Scaling the thrust and deformations of a rotor with flexible blades. *Physical Review Fluids*, 8(4), 2023.

[44] WA Timmer. Two-dimensional low-reynolds number wind tunnel results for airfoil naca 0018. *Wind Engineering*, 32(6):525–537, 2008.

[45] Stefan Hoerner, Shokoofeh Abbaszadeh, Thierry Maître, Olivier Cleynen, and Dominique Thévenin. Characteristics of the fluid–structure interaction within darrieus water turbines with highly flexible blades. *Journal of Fluids and Structures*, 88:13–30, 2019.

[46] Brian Hand, Ger Kelly, and Andrew Cashman. Aerodynamic design and performance parameters of a lift-type vertical axis wind turbine: A comprehensive review. *Renewable and Sustainable Energy Reviews*, 139:110699, 2021.

[47] Omar S Mohamed, Ahmed MR Elbaz, and Alessandro Bianchini. A better insight on physics involved in the self-starting of a straight-blade darrieus wind turbine by means of two-dimensional computational fluid dynamics. *Journal of Wind Engineering and Industrial Aerodynamics*, 218:104793, 2021.

[48] Jr. Anderson, John D. and Christopher P. Cadou. *Fundamentals of Aerodynamics*. McGraw-Hill Education, 7 edition, 2023.